OPEN ACCESS

Stack-like Contacting in Solid Oxide Cells: Electrochemical Characterization and Modeling

Journal of The Electrochemical Society, 2024 **171** 044506

Stack-like Contacting in Solid Oxide Cells: Electrochemical Characterization and Modeling

D. Ewald,[1,z] C. Grosselindemann,[1,*] D. Esau,[1,*] F.-M. Fuchs,[2] and A. Weber[1,]**

[1]*Institute for Applied Materials—Electrochemical Technologies (IAM-ET), Karlsruhe Institute of Technology (KIT), Karlsruhe, D-76131, Germany*
[2]*Kerafol Keramische Folien GmbH & Co. KG, Koppe-Platz 1, Eschenbach, D-92676, Germany*

The integrity of metallic interconnectors (MICs) in a solid oxide cell stack is crucial because contact resistances or limitations in gas supply may occur. In this contribution, a Crofer 22 APU® interconnector with a (Mn, Co, Fe)$_3$O$_4$ spinel oxide (MCO) coating and a lanthanum-strontium-manganese-cobalt oxide (LSMC) contact layer at the air side was investigated. The electrochemical behavior was characterized by means of IV-characteristics, impedance spectroscopy and DRT analysis. In particular, the contact losses at the air side were measured with targeted potential probes. With respect to the contact layer mounted in a dried state, the application of a stack-like clamping pressure of 1 MPa showed a significant decrease of the contact resistance. In order to extend an existing zero-dimensional performance model for an electrolyte-supported cell with a Ni/GDC fuel electrode and LSCF air electrode, a method was established to parameterize contact losses at the air electrode. The observed activation energy of the contact losses showed to be independent of the clamping pressure. Additionally, the dependency of the cell´s intrinsic ohmic losses towards the steam partial pressure at the Ni/GDC fuel electrode was quantified and included to the model. Simulation studies were validated with experimental data for technical operating conditions.

 [DOI: 10.1149/1945-7111/ad3a16]

Manuscript submitted February 2, 2024; revised manuscript received March 21, 2024. Published April 16, 2024. *This paper is part of the JES Focus Issue on SOFC XVIII: Advances in Solid Oxide Fuel Cell and Electrolysis Cell Technology.*

List of Symbol

Latin letters

a	exponent describing hydrogen partial pressure dependency of the fuel electrode's exchange current density (-)
b	exponent describing steam partial pressure dependency of the fuel electrode's exchange current density (-)
B_{ohm}	specific constant for ohmic resistance (K (Ω m^2)$^{-1}$)
D_i	diffusion coefficient of species i (m^2 s^{-1})
G	geometry parameter (m^{-1})
j	current density (A m^{-2})
$j_{0,EL}$	exchange current density (A m^{-2})
m	exponent describing oxygen partial pressure dependency of the air electrode's exchange current density (−)
$p_{clamping}$	clamping pressure (Pa)
p_i	partial pressure of species i (atm)
R	area specific resistance (Ω m^2)
$R_{0,MIC}$	overall ohmic resistance (Ω m^2)
T	temperature (K)
U	voltage (V)
z	number of exchanged electrons (-)

Greek letters

α	charge transfer coefficient (-)
Δ	difference
γ	exponential prefactor (A m^{-2})
η	overpotential (V)
φ	potential (V)
Ψ	microstructure parameter (-)

Subscripts

0	ohmic
AE	air electrode
act	activation
cell	cell
contact	contact
corr	correction
diff	diffusion
EL	electrode
eff	effective
FE	fuel electrode
H_2	hydrogen
H_2O	steam
inert	inert gas
MIC	metallic interconnector
OCV	open circuit voltage
ohm	ohmic
pol	polarization
probe	probe
ref	reference
SOEC	solid oxide electrolysis cell

Constants

F	faraday constant 96485 (A s mol^{-1})
p_{corr}	conversion factor 101330 (Pa atm^{-1})
p_{ref}	reference pressure 1 (atm)
$\tilde{R}$	universal gas constant 8.314 (J mol^{-1} K^{-1})

Metallic interconnectors (MICs)[1–3] in stacks with high temperature solid oxide cells (SOCs)[4] are essential components in order to realize high-scaled production of hydrogen (H_2) and/or mixtures of hydrogen and carbon monoxide (synthesis gas).[5–8] The application of steel grades for MICs in commercialized stacks[9] is economically beneficial since material and manufacturing costs are significantly lower compared to ceramic flow fields.[10] MICs are usually made of ferritic steels, as for example Crofer 22 APU®, which can meet the thermal expansion requirement and exhibit the ability to form a conductive chromium (Cr) oxide layer.

However, chromium poisoning of the air electrode reduces the cell performance.[11,12] Due to this, a protective coating needs to be applied onto the MIC at the air side.[13] Various coating types as oxides with reactive elements, perovskites and spinels are available,[2] that can be applied with different coating techniques.[14–18]

In addition, a protective coating is beneficial in order to reduce contact losses between the MIC and air electrode.[19–22] Still, an

*Electrochemical Society Student Member.
**Electrochemical Society Member.
[z]E-mail: daniel.ewald@kit.edu

additional Cathode (air electrode) Contact Layer (CCL) can be applied to minimize the contact losses.[17,23–26] Such a CCL can also level out insufficient contacting due to surface roughness related to manufacturing of the MIC and air electrode.[27] Here, contact pastes can be used which are initially applied onto the MIC or air electrode before stacking.[28,29] In a previous work, a liquid contact paste made of lanthanum-strontium-cobalt-iron oxide (LSCF) applied by screen-printing onto the air electrode was used in combination with a physical vapor deposition (PVD) cerium cobalt (CeCo) coated MIC in order to optimize the cell performance.[19]

In this work, a single cell test setup with a stack-like contacting concept using Crofer 22 APU® as MIC material is investigated. At the air side a protective coating of manganese-cobalt based spinel oxide (MCO) is applied onto the MIC. In literature, Gruenwald et al.[15] observed a self-healing behavior when using such a coating applied by atmospheric plasma spraying (APS). Montero et al.[21] showed that a screen-printed MCO coating on a Crofer 22 APU® MIC significantly reduced the contact losses at the air side. Further, no chromium compounds were found in either the air electrode or contact layer after 1 kh test procedure. Long-term stability for 40 kh SOFC-operation was shown in Ref. 24.

In terms of contacting the air electrode with the MIC, a CCL made of lanthanum-strontium-manganese-cobalt oxide (LSMC) was in advance screen-printed onto the air electrode and dried afterwards, resulting in a dry contact layer in this work. This simplifies the stacking process as stacking with cells exhibiting a liquid contact paste is rather challenging. The interaction between an LSMC CCL and MCO coated MIC is shown in Ref. 30.

However, stack-like contacting undergoes with degradation effects like Cr-poisoning,[11,31–34] corrosion,[35,36] increased contact resistances[19,28,37] and limitations in gas supply. Thus, SOCs were investigated on cell level[38,39] in an inert testing environment with ceramic flow fields and contacted with finely meshed grids in order to observe the cell-intrinsic electrochemical behavior.[40–42] Under those ideal conditions, electrochemical characterization has been shown for various cell types such as anode-supported cells (ASCs)[38,40,41,43] and electrolyte-supported cells (ESCs).[44–46]

Within the scope of this contribution, an existing impedance-based zero-dimensional dc performance model[45] for an ideally contacted ESC consisting of a nickel/gadolinia-doped ceria (Ni/GDC) fuel electrode, 3-mol. % yttria-stabilized zirconia (3YSZ) electrolyte[47] and an LSCF air electrode is adjusted and extended to stack-like conditions. Here, a new methodology is established to further parameterize cell-intrinsic ohmic losses and contact losses at the air side separately from each other with respect to stack-like contacting. Additionally, the dependency of the cell-intrinsic ohmic losses towards the steam partial pressure at the Ni/GDC fuel electrode is quantified and included to the model, since the conductivity of GDC has a dependence on the oxygen partial pressure.[48,49]

To parameterize the zero-dimensional cell model for stack-like conditions, an electrochemical characterization was carried out by using IV-characteristics and electrochemical impedance spectroscopy (EIS) under technically relevant conditions in electrolysis mode. In addition, contact losses between air electrode and coated MIC are measured with targeted potential probes according to the method by Kornely et al.[20]

Further on, the influence of the clamping pressure towards the cell performance and contact losses at the air electrode is investigated when using a dry contact layer. Thereby, a stack-like clamping pressure of 1 MPa is applied to the active cell area.

Finally, the simulated cell voltage and contact losses at the air electrode are validated over a wide technically relevant SOEC operating range with experimental data.

Methods

In the following section, the zero-dimensional performance model including the underlying mathematical expressions for the respective loss processes will be discussed for a planar electrolyte-supported cell that is contacted by metallic flow fields as used in this study.

Modeling.—For describing the current-voltage behavior of the SOC a zero-dimensional dc performance model was used, which is based on an open circuit voltage (OCV) minus losses model.[43] Herein, the cell voltage U_{cell} at a specific current density j is calculated by subtracting ohmic losses η_{ohm}, activation losses at the fuel electrode (FE) $\eta_{\text{act,FE}}$ and air electrode (AE) $\eta_{\text{act,AE}}$ as well as gas diffusion losses at the fuel electrode $\eta_{\text{diff,FE}}$ and air electrode $\eta_{\text{diff,AE}}$ from the open circuit voltage U_{OCV} in Eq. 1. The equations are given in Refs. 43 and 50. Such a model was applied by Grosselindemann et al.[45] to an identical cell tested with an ideal contacting setup.

$$U_{\text{cell}} = U_{\text{OCV}} - \eta_{\text{ohm}} - \eta_{\text{act,FE}} - \eta_{\text{act,AE}} - \eta_{\text{diff,FE}} - \eta_{\text{diff,AE}} \quad [1]$$

Ohmic losses can be attributed to electronic and ionic charge transport and represent the proportionality between the current density j and the area-specific ohmic resistance R_{ohm} in Eq. 2.

$$\eta_{\text{ohm}} = j \cdot R_{\text{ohm}} \quad [2]$$

As the ohmic losses in planar, electrolyte-supported single cells are commonly determined by the electrolyte, a suitable description for the dependency of the ohmic resistance towards the temperature can deliver an Arrhenius approach with the temperature T and the universal gas constant $\tilde{R}$ in Eq. 3. This requires the determination of the cell specific parameter B_{ohm} and the ohmic activation energy $E_{\text{act,ohm}}$.

$$R_{\text{ohm}} = \frac{T}{B_{\text{ohm}}} \cdot \exp\left(\frac{E_{\text{act,ohm}}}{\tilde{R}T}\right) \quad [3]$$

Regarding stack-like contacting with MICs, contact losses at the respective electrodes are ohmic,[20] thus ohmic losses from Eq. 2 have to be split up into cell-intrinsic ohmic losses $\eta_{\text{ohm,cell}}$, contact losses at the fuel electrode $\eta_{\text{ohm,contact,FE}}$ and air electrode $\eta_{\text{ohm,contact,AE}}$ in Eq. 4.

$$\eta_{\text{ohm}} = \eta_{\text{ohm,cell}} + \eta_{\text{ohm,contact,FE}} + \eta_{\text{ohm,contact,AE}} \quad [4]$$

Contact losses at the fuel electrode are negligibly small when a Ni-mesh is properly spot-welded onto the MIC and a Ni-rich contact layer ensuring a metallic contact towards the Ni-mesh is applied.[20] The surface layer of the MIC at the air side consists of metal oxides due to the oxidizing gas atmosphere conditions prevailing there. The electronic conductivity of such layers is therefore thermally activated.[37] Consequently, the Arrhenius approach in Eq. 3 is also applicable to describe the temperature dependency of the contact resistance at the air electrode. If the total ohmic resistance $R_{\text{ohm,cell}} + R_{\text{ohm,contact,AE}}$ is determined by impedance spectroscopy, Eq. 3 might be applied using an effective ohmic activation energy and cell specific parameter.

Activation losses caused by charge transfer reactions can be quantified by using the Butler-Volmer approach in Eq. 5. Here, $j_{0,EL}$ corresponds to the exchange current density and α_{EL} the charge transfer coefficient of the respective electrode (EL). Further, z denotes the number of exchanged electrons and F the Faraday-constant.

$$j = j_{0,EL}\left[\exp\left(\alpha_{EL}\frac{zF\eta_{\text{act},EL}}{\tilde{R}T}\right) - \exp\left(-(1-\alpha_{EL})\frac{zF\eta_{\text{act},EL}}{\tilde{R}T}\right)\right] \quad [5]$$

The exchange current density is shown in Eqs. 6 and 7 for the fuel and air electrode, respectively. Here, p_{ref} denotes the reference pressure of 1 atm, $p_{\text{H}_2,\text{FE}}$ the hydrogen partial pressure at the fuel electrode, $p_{\text{H}_2\text{O,FE}}$ the steam partial pressure at the fuel electrode and

$p_{O_2,AE}$ the oxygen partial pressure at the air electrode. It should be noted that the influence of the overall pressure can be neglected here since all experiments were carried out under atmospheric pressure. Furthermore, a, b and m correspond to dimensionless exponents as well as γ_{EL} an exponential pre-factor and $E_{act,EL}$ the activation energy of the respective electrode.

$$j_{0,FE} = \gamma_{FE}\left(\frac{p_{H_2,FE}}{p_{ref}}\right)^a\left(\frac{p_{H_2O,FE}}{p_{ref}}\right)^b \exp\left(-\frac{E_{act,FE}}{\tilde{R}T}\right) \quad [6]$$

$$j_{0,AE} = \gamma_{AE}\left(\frac{p_{O_2,AE}}{p_{ref}}\right)^m \exp\left(-\frac{E_{act,AE}}{\tilde{R}T}\right) \quad [7]$$

Gas diffusion losses can be derived by using Fick's law in combination with the Nernst equation, ideal gas law and first Faraday's law as in Refs. 51 and 52. The resulting gas diffusion losses at the fuel and air electrode are shown in Eqs. 8 and 9, respectively. Here, L_{EL} denotes the gas diffusion length which is usually set to the thickness of the corresponding electrode,[43,45] Ψ_{EL} the microstructure parameter, D_i the gas diffusion coefficient of the species i, $p_{i,EL}$ the partial pressure of the species i at the respective electrode and P_{corr} a conversion factor of 101330 Pa atm^{-1}.

$$\eta_{diff,FE} = \frac{\tilde{R}T}{2F}\ln\left(\frac{1 + \frac{\tilde{R}TL_{FE}}{2F\psi_{FE}D_{H_2O}p_{H_2O,FE}P_{corr}}\cdot j}{1 - \frac{\tilde{R}TL_{FE}}{2F\psi_{FE}D_{H_2}p_{H_2,FE}P_{corr}}\cdot j}\right) \quad [8]$$

$$\eta_{diff,AE} = \frac{\tilde{R}T}{4F}\ln\left(\frac{1}{1 - \frac{\tilde{R}TL_{AE}\left(1 - p_{O_2,AE}/p\right)}{4F\psi_{AE}D_{O_2}p_{O_2,AE}P_{corr}}\cdot j}\right) \quad [9]$$

Considering the investigated electrolyte-supported cells with electrode thicknesses below 30 µm, gas diffusion in the electrodes can be neglected and the observed gas diffusion resistance has to be attributed to the two-dimensional gas diffusion in the Ni-contact grid at the fuel electrode and contact layer at the air electrode. Here it has to be considered that in-plane gas diffusion underneath the contact ribs will have a significant impact.[53]

Experimental.—Electrolyte-supported cells with an active cell area of 1 cm^2 were analyzed in this contribution. The cells consist of a 85 µm thick[45] 3-mol. % yttria-stabilized zirconia (3YSZ) electrolyte with a nickel/gadolinia-doped ceria (Ni/GDC) fuel electrode and LSCF air electrode. Additionally, GDC layers are placed between the electrolyte and electrodes. Further details about the cell are given in Ref. 45.

Measurements were carried out with full cells by using a test rig as described in Refs. 54 and 55. At the fuel side a total flow rate of 250 sccm was set. Several steam contents can be realized by mixing oxygen to the fuel using an upstream combustion chamber. Steam partial pressures between 0.35 and 0.80 atm with a step width of 0.15 atm in a temperature range between 775 and 850 °C (25 °C step width) were investigated. Since only electrolysis mode is considered in this contribution, pure oxygen was used at the air side with a flow rate of 50 sccm for the electrochemical characterization. According to Eq. 9, gas diffusion losses at the air electrode become zero under these conditions. However, in order to be able to compare the measurements with the results from a previous work,[19] a flow rate of 250 sccm air was set at the air electrode as it was also the case there.

A predefined startup procedure was performed after the cell has been mounted into the test bench. Sealing is ensured by a gold frame which is placed between electrolyte and ceramic housing at the air side. Gas leakages were determined via the measured OCV by calculating back the increase in steam partial pressure in the fuel. This procedure revealed minor increases of the steam contents (⩽1.75 %) in all tests, proving that the gold frame enables an adequate sealing. It should be noted that active cell area and sealing are mechanically decoupled and the specified clamping pressures are only acting onto the active cell area as shown in Ref. 54. The housing and gold sealant are compressed by additional Al_2O_3-weights (1.2 kg), thus the sealing is not influenced by clamping pressure of the contact area. IV-characteristics and impedance measurements were conducted by systematically varying operating parameters. The measured spectra were acquired by a Zahner Zennium E frequency response analyzer in galvanostatic mode and the excitation amplitude is chosen to receive a voltage response with an amplitude ⩽12 mV regarding the polarization resistance.[54] A frequency range between 30 mHz and 100 kHz with 12 points per decade was chosen. All spectra were measured without bias current.

The quality of the measured spectra was evaluated by using the Kramers Kronig validity test,[56] revealing errors ⩽1.5 %. Furthermore, the polarization resistance at identical operating conditions both between start and end of characterization as well as among identical cells differs ⩽5 % from each other. Changes in ohmic resistance between the start and end of electrochemical characterization (in the time range of approximately 300 h) are ⩽2.5 % and therefore neglectable.

Ideal contacting is realized by using finely meshed double-layered contact grids consisting of gold at the air side and nickel at the fuel side. Ceramic-based (Al_2O_3) flow fields and cell housing further on provide an inert testing environment. Occurring contact losses resulting from this setup can be neglected.[40,45,54] Gas transport conditions are illustrated schematically in Fig. 1a and described in more detail in Ref. 45.

Metallic interconnectors made of Crofer 22 APU® were used for stack-like contacting as shown schematically in Fig. 1b. A single-

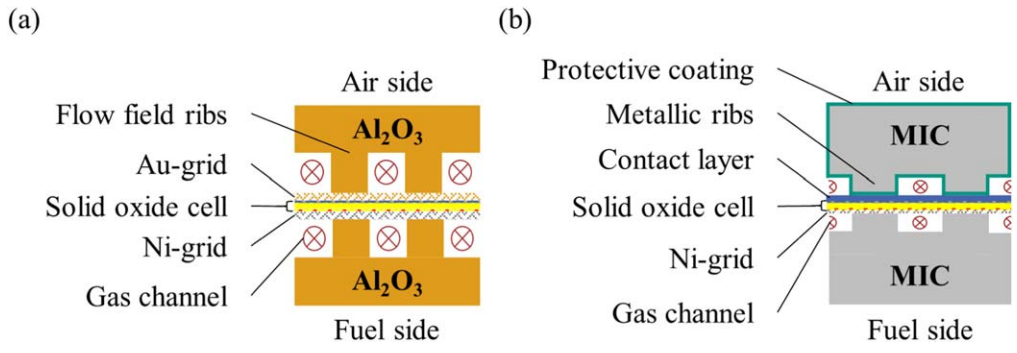

Figure 1. (a) Ideal contacting with ceramic flow fields (made of Al_2O_3) and contact grids consisting of Ni (fuel side) and Au (air side) and (b) stack-like contacting design with metallic interconnectors (MIC) made of Crofer 22 APU®, Ni-contact grid (fuel side), contact layer (air side) and protective MCO coating on the MIC at the air side.

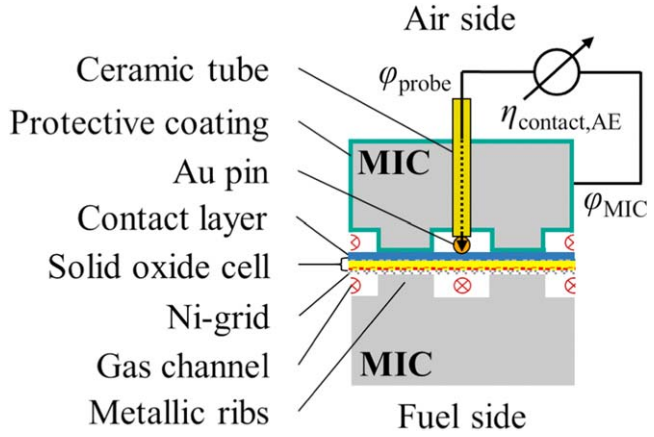

Figure 2. Contact loss measurement at the air electrode according to Kornely et al.[20] with targeted potential probes for stack-like contacting.

layered nickel grid that has been spot-welded onto the MIC was used to contact the fuel electrode. Regarding the air side, a protective coating on the MIC is necessary to prevent the air electrode from Cr poisoning. In this work, a (Mn, Co, Fe)$_3$O$_4$ spinel oxide (MCO) coating was used for the MIC at the air side. Furthermore, a contact layer is placed between the MCO coated MIC and air electrode to further reduce occurring contact losses. In this contribution a dry contact layer consisting of lanthanum-strontium-manganese-cobalt oxide (LSMC), that had already been screen-printed onto the air electrode and dried afterwards, was used since this simplifies the stacking process in contrast to mounting the cell with a contact paste still in liquid phase. Thus, the contact between the LSMC layer and MCO coated MIC is initially dry in this work. Nevertheless, mounting the cell with an LSCF contact paste in the liquid state as shown in Ref. 19 is also used in this study as a benchmark and for reference purposes.

According to Kornely et al.,[20] contact losses at the air electrode $\eta_{contact,AE}$ can be quantified using targeted potential probes as shown in Fig. 2. This is realized by inserting a ceramic capillary tube with a gold wire inside through the drilling of the MIC at the air side. Thus, the potential of the air electrode φ_{probe} can be measured by the gold pin touching the surface of the air electrode. In addition, with the potential of the MIC at the air side φ_{MIC}, the resulting contact losses can be calculated according to Eq. 10 by forming the difference between both potentials. According to Geisler et al.,[57] the electronic potential in the air electrode is approximately equal and in-plane ohmic losses can be neglected for highly conductive LSCF air electrodes and channel widths below 1 mm. Thus, the measured $\eta_{contact,AE}$ is not affected by in-plane ohmic losses in the air electrode.

$$\eta_{contact,AE} = \varphi_{MIC} - \varphi_{probe} \quad [10]$$

Similarly, this can be done at the fuel side as described in Refs. 19 and 20. However, contact losses at the fuel electrode are negligibly small in this set-up since a nickel grid is used comparably to the ideal contacting case.[19] Due to this, these are not considered further below.

To ensure an adequate contact between electrode and MIC on both the fuel and air side, weights are used, which rest on a ceramic capillary as shown in Fig. 3b outside the furnace above the test bench. This ceramic capillary is pressing downwards onto the MIC at the air side as illustrated in Fig. 3a. In a former work where an initially liquid LSCF paste was used as a contact layer,[19] a contact pressure of approximately 0.05 MPa (500 g contact weight) was applied. However, clamping pressures of several MPa are prevailing within a commercialized stack. In order to investigate the influence of the clamping pressure to the contact losses at the air side when using a dry LSMC CCL, an increase to a rather stack-like clamping pressure of approximately 1 MPa was achieved by a modification of the test bench, which corresponds to a contact weight of 10 kg. When mounting the cell into the test bench, any height differences between the ceramic housing and MIC must be taken into account when a clamping pressure of 1 MPa is applied. Otherwise, the cell could be damaged or, in the worst case, break. If this height difference adjustment between MIC and ceramic housing is precisely done, no mechanical damage to the cell was detected after removal from the test bench. However, since only ESCs were examined in this study, it is uncertain whether such an increased clamping pressure could also be applied to ASCs without leading to a mechanical failure. This needs to be analyzed in further studies.

Under both clamping pressures used Ni-grids, which are contacted with the MIC at the fuel side, were analyzed post-mortem by a Keyence VHX-7000 digital microscope in order to obtain color mapped height profiles shown in the Appendix.

Results and Discussion

In the following section, the impact of the coating and CCL on the performance is shown by measured IV-curves in electrolysis mode. Measurements from a previous work[19] are used for reference purposes.

IV-Characteristics.—In Fig. 4 the performance of the MIC-contacting applied in this study is compared to previous results. The IV-curves from Ref. 19 showed that ideal contacting with gold mesh and ceramic flow field at the air electrode enables the highest performance. In contrast to this, uncoated Crofer 22 APU® MICs with an LSCF contact paste at the air side showed the lowest performance. Coating the MIC at the air side with MCO enables

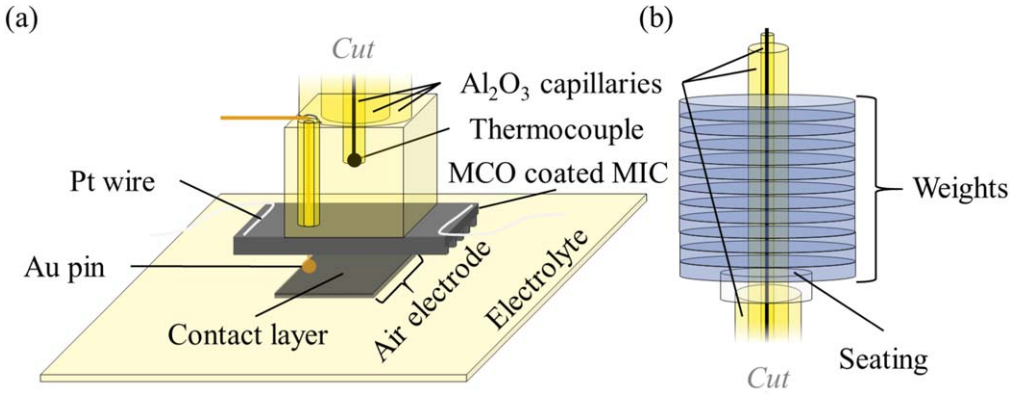

Figure 3. (a) Realizing clamping pressures by a ceramic capillary pressing downwards onto the MIC at the air side with (b) contact weights at the top of the test bench.

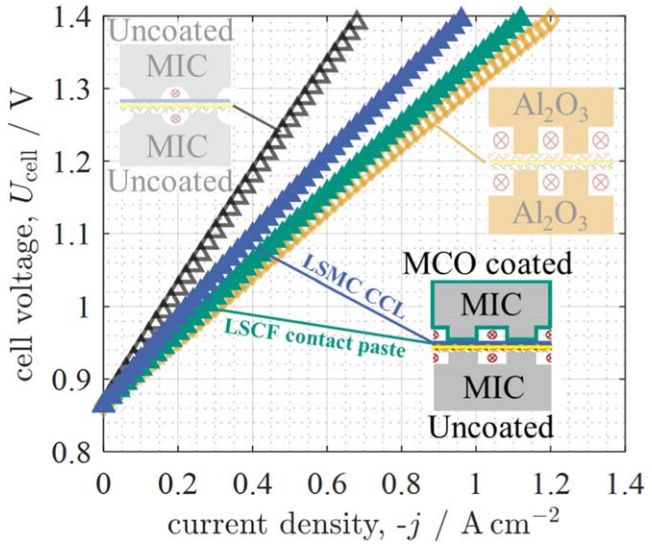

Figure 4. IV-characteristics of an MCO coated MIC at the air side with an LSMC CCL and LSCF contact paste in comparison with measurements from a previous work[19] (ideal contacting and stack-like contacting with uncoated MICs and LSCF contact paste at the air side) in electrolysis mode at $T = 850$ °C with 0.80 atm H_2O (balanced H_2), air at the air electrode and a clamping pressure of 0.05 MPa (MIC = Crofer 22 APU®).

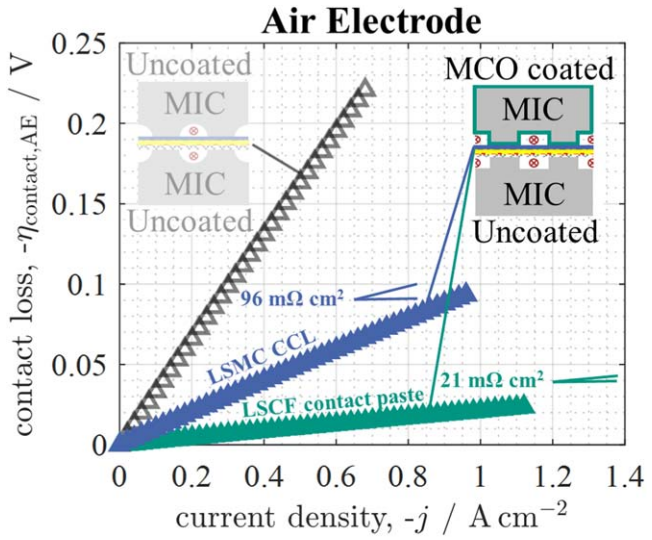

Figure 5. Contact losses of MCO coated MIC with an LSMC CCL and LSCF contact paste at the air side in comparison with measurements from a previous work[19] (stack-like contacting with uncoated MICs and LSCF contact paste at the air side) in electrolysis mode at $T = 850$ °C with 0.80 atm H_2O (balanced H_2), air at the air electrode and a clamping pressure of 0.05 MPa(MIC = Crofer 22 APU®).

performance values quite similar to ideal contacting, as in the case when using a CeCo coating in a previous work,[19] which can be attributed to improved contacting and reduced chromium poisoning.

Replacing the LSCF contact paste with a dry LSMC contact layer between the MCO coated MIC and air electrode leads to a slightly lower performance within this benchmark window, as shown in Fig. 4. Quantitatively, the use of a dry LSMC contact layer increases the cell voltage by 5 % at -0.8 A cm^{-2} in comparison to an LSCF contact paste. A possible cause for this might be increased contact losses at the air electrode due to the dry contact layer, which is discussed in the following section.

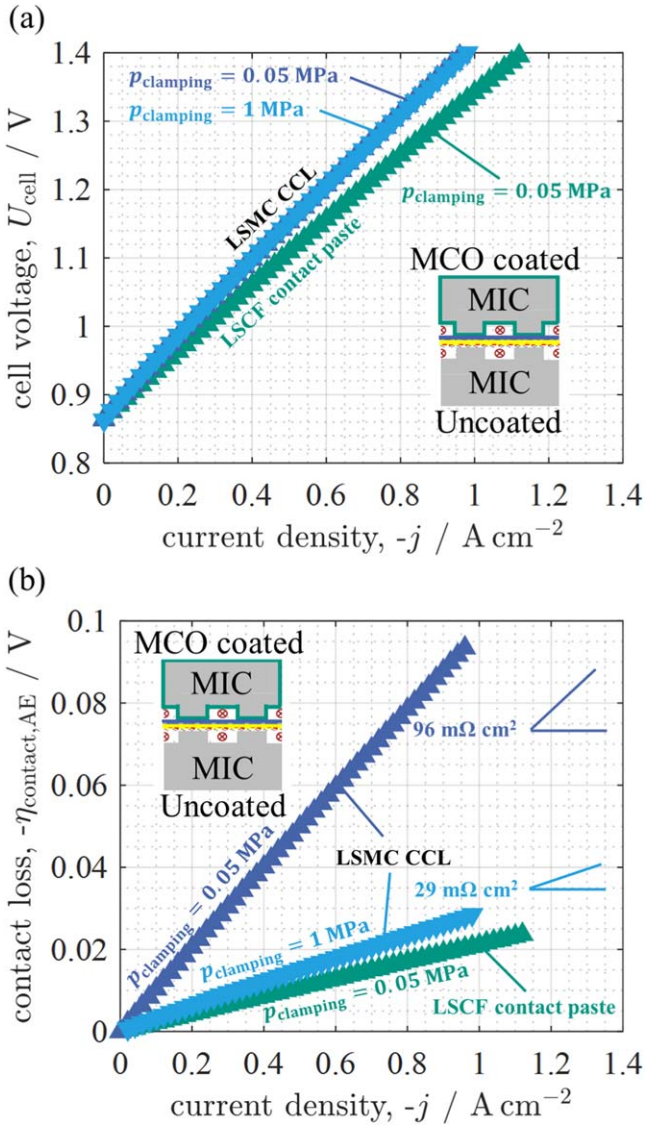

Figure 6. (a) IV-characteristics and (b) contact loss measurements at the air side of MCO coated MIC with different contact layers and increased clamping pressure concerning the LSMC contact layer in electrolysis mode at $T = 850$ °C with 0.80 atm H_2O (balanced H_2) and air at the air electrode (MIC = Crofer 22 APU®).

Contact losses at air side.—While contact losses at the air side are neglectable in terms of ideal contacting where a gold grid is used (<3 mΩ cm^2),[42] these must be taken into account for stack-like contacting. Therefore, additional investigations with targeted measurements of potential probes at the air side were carried out in order to quantify the contact losses. Regarding the fuel side, occurring contact losses between fuel electrode and Ni-grid are negligibly small (<5 mΩ cm^2) and therefore not considered here.

Figure 5 shows voltage losses at the air side in electrolysis mode due to contacting at $T = 850$ °C with 0.80 atm H_2O (balanced H_2) and air at the air electrode. In general, a coating on the MIC at the air side can reduce contact losses significantly. The contact losses at the air side of the MCO coated MIC show an almost identical behavior as the CeCo coating from previous work[19] when using each an LSCF contact paste. Replacing the LSCF contact paste by a dry LSMC contact layer leads to a significant increase in contact losses, as shown in Fig. 5. By assuming that contact losses at the air side are solely ohmic, the resulting contact resistance can be obtained from the respective slope. Thereby, the contact resistance increased from 21 to 96 mΩ cm^2. The increase in

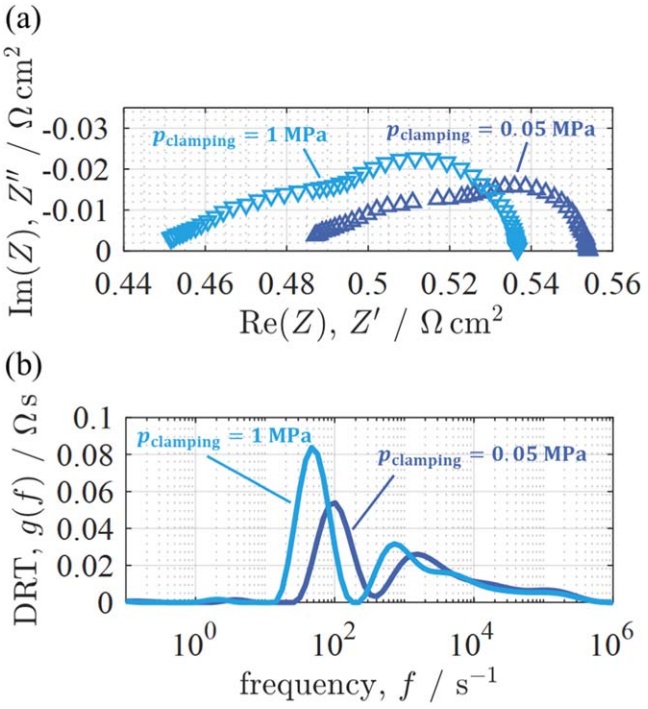

Figure 7. (a) Impedance spectra and (b) DRT of MCO coated MIC with LSMC contact layer at the air side and a clamping pressure of 0.05 and 1 MPa at $T = 850$ °C with 0.80 atm H_2O (balanced H_2) and oxygen at the air electrode (MIC = Crofer 22 APU®).

voltage loss at -0.8 A cm^{-2} is approximately 60 mV, which corresponds to the performance difference in Fig. 4. The lower performance in the case of a dry LSMC contact layer is therefore solely attributed to the increased contact losses at the air side.

So far, the results shown above were generated with an applied clamping pressure of 0.05 MPa. In terms of an LSMC CCL mounted after drying, the influence of the clamping pressure towards the performance and contact losses at the air side will be investigated in the following. Therefore, a clamping pressure of 1 MPa is applied in order to reduce contact losses at the air side in case of using such an initially dry LSMC contact layer.

Influence of clamping pressure.—An increase in clamping pressure from 0.05 to 1 MPa seems to have no impact on the overall performance, as shown in Fig. 6a. In contrast to this, in Fig. 6b contact losses at the air side are significantly reduced through the increase to 1 MPa clamping pressure. Quantitatively, the contact resistance obtained from the slope in Fig. 6b decreased by a factor of approximately three and is now on a similar level as when an LSCF contact paste is used as a contact layer at 0.05 MPa. Since the performance remains constant while the contact losses at the air side decreased, other loss contributions must have increased. For quantification, an impedance analysis is conducted in the following section.

Impedance analysis.—Ohmic resistance decreased through the increase in clamping pressure from 486 to 450 mΩ cm^2, as illustrated in Fig. 7a. However, the resulting difference of 36 mΩ cm^2 does not correspond to $\Delta R_{contact,AE} = (96 - 29)$ mΩ cm^2 = 67 mΩ cm^2 in Fig. 6b. Accordingly, the cell-intrinsic ohmic resistance appears to have increased by 31 mΩ cm^2 through the increase in clamping pressure. However, this is in the range of the standard deviation of cell-intrinsic ohmic resistance (±33 mΩ cm^2) between tested identical cells. Therefore, this increase can most probably be attributed to manufacturing and cell-mounting related variations between both tested cells. In addition, the polarization resistance increased from 69 to 86 mΩ cm^2, as shown in Fig. 7a. Through the higher clamping pressure, several peaks between 1 and 10^4 s^{-1} increased and are shifted towards lower frequencies as can be seen in the DRT in Fig. 7b. As pure oxygen is used at the air side, gas diffusion is avoided and consequently not considered. Therefore, one possible reason for the increased polarization resistance might be a compression of the Ni-mesh, leading to an increased gas diffusion resistance at the fuel electrode. However, the gas diffusion process at the fuel electrode is to be quantified in the

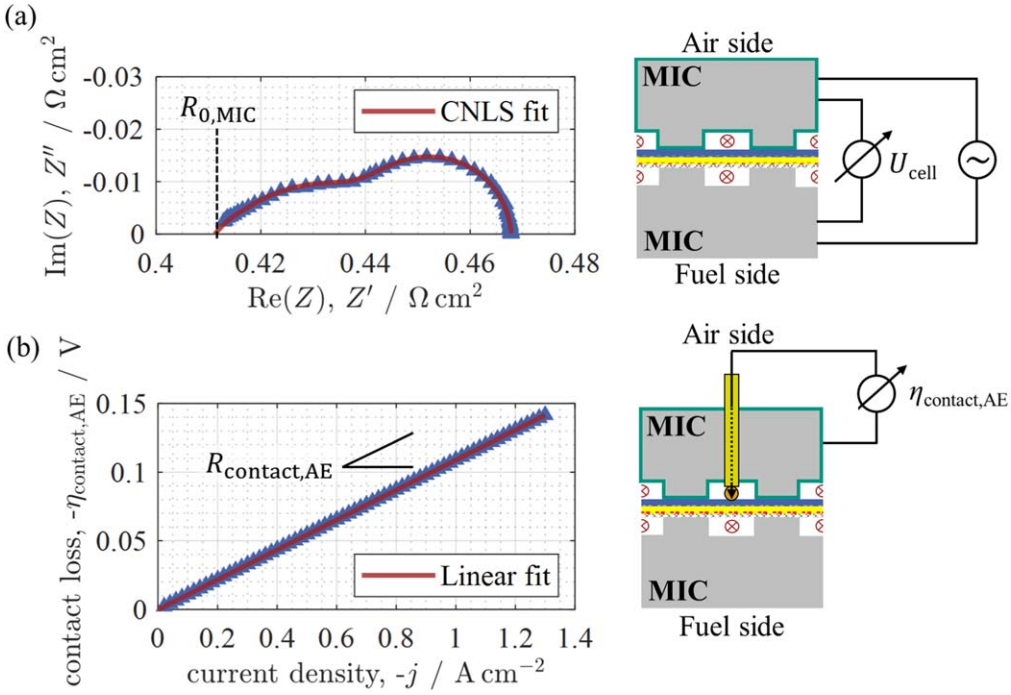

Figure 8. (a) Obtained overall ohmic resistance $R_{0,MIC}$ from EIS measurements and (b) determined contact resistance $R_{contact,AE}$ from contact loss measurement with targeted potential probes at the air side at $T = 850$ °C with 0.80 atm H_2O (balanced H_2) and oxygen at the air electrode with a clamping pressure of 0.05 MPa.

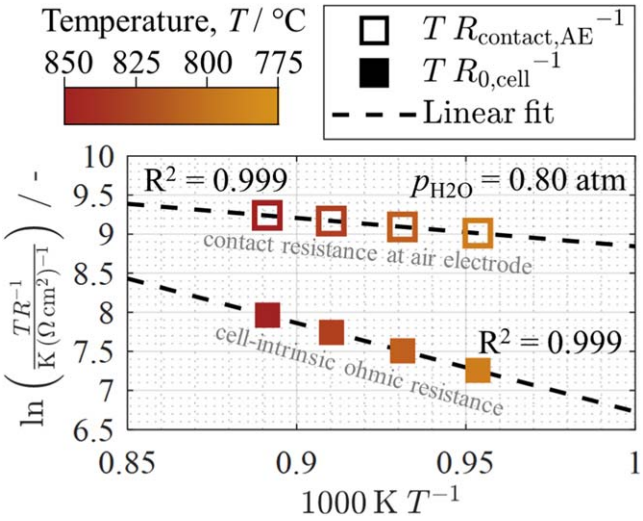

Figure 9. Exemplary Arrhenius plot for cell-intrinsic ohmic resistance and contact resistance at the air side at 0.80 atm H_2O (balanced H_2) at the fuel electrode and oxygen at the air electrode with a clamping pressure of 0.05 MPa.

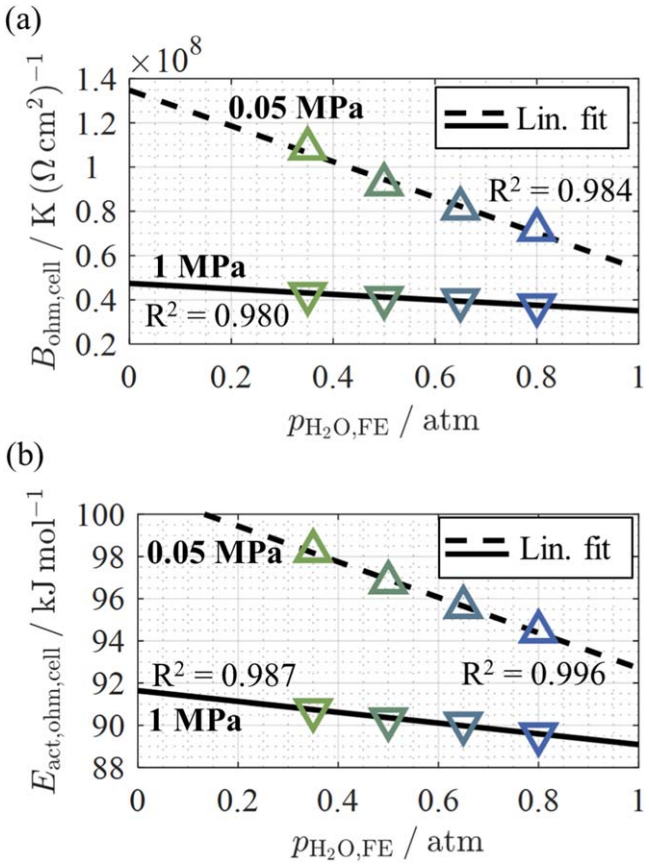

Figure 10. Dependency of the cell-intrinsic (a) ohmic parameter $B_{ohm,cell}$ and (b) ohmic activation energy $E_{act,ohm,cell}$ towards the steam partial pressure at the fuel electrode for both clamping pressures with performed linear fits for 775 °C ⩽ T ⩽ 850 °C and 0.35 atm ⩽ $p_{H2O,FE}$ ⩽ 0.80 atm. Obtained fit values are listed in Table I.

Appendix and compared between both applied clamping pressures. Summarized, the gas diffusion resistance at the fuel electrode was increased and light microscopic images confirmed that the Ni-mesh has been compressed through the increase in clamping pressure. Since the increased clamping pressure may also affect the gas diffusion process at the air electrode, it is further shown that the gas diffusion resistance

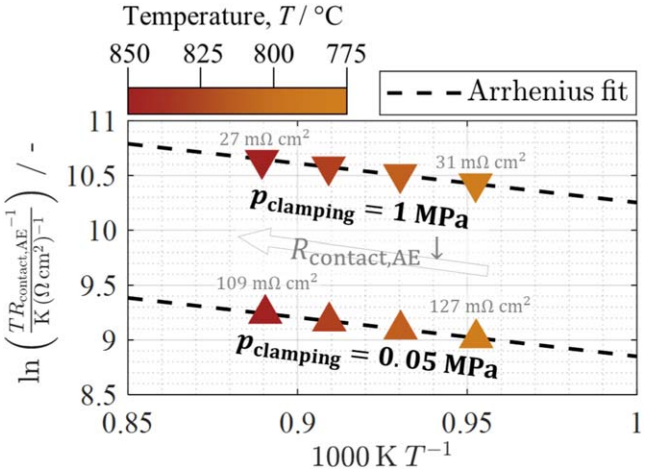

Figure 11. Over $p_{H2O,FE}$-averaged contact resistances at the air electrode and the corresponding Arrhenius fit for a clamping pressure of 0.05 and 1 MPa between 775 °C ⩽ T ⩽ 850 °C (plotted according to Eq. 13, parameters are listed in Table II).

increased similarly as at the fuel electrode. One possible cause here might be an enhanced sintering/compression and densification of the porous contact layer through the higher clamping pressure.

Parameterization.—In this section the parameterization for the given zero-dimensional performance model[45] is carried out in order to extend it to stack-like conditions. Thereby, only the stack-like contacting setup with the dry LSMC contact layer at the air side is considered with both applied clamping pressures.

To parameterize cell-intrinsic ohmic losses and contact losses at the air side separately from each other, a new approach is presented in this work. Therefore, impedance analysis and contact loss measurements at the air side are combined. The overall ohmic resistance $R_{0,MIC} = R_{0,cell} + R_{contact,AE}$ can be obtained from the intercept of the real part axis in the Nyquist plot based on a CNLS fit of the spectra with RQ-elements for R_{pol} and serial element for ohmic losses as shown in Fig. 8a. Here, it should be noted that $R_{0,MIC}$ includes besides the cell-intrinsic ohmic resistance also the contact resistance at the air electrode, since EIS measurements are conducted via both MICs at the fuel and air side as illustrated in Fig. 8a in the sketch on the right side. With the assumption that occurring contact losses at the air side are solely ohmic, the contact resistance can be determined by the slope from the contact loss measurement in Fig. 8b according to Eq. 11.

Since contact losses at the fuel side are negligibly small, it is therefore possible to quantify the cell-intrinsic ohmic resistance $R_{0,cell}$ by subtracting the contact resistance at the air side $R_{contact,AE}$ from the overall ohmic resistance $R_{0,MIC}$ obtained from EIS measurements as shown in Eq. 12.

$$R_{contact,AE} = \frac{\partial \eta_{contact,AE}}{\partial j} \quad [11]$$

$$R_{0,cell} = R_{0,MIC} - R_{contact,AE} \quad [12]$$

In order to parameterize the respective ohmic loss contribution i, the Arrhenius' approach from Eq. 3 is rearranged according to the following Eq. 13.

$$\ln\left(\frac{T\,R_{0,i}(T)^{-1}}{\mathrm{K\,(\Omega\,cm^2)^{-1}}}\right) = \ln\left(\frac{B_{ohm,i}}{\mathrm{K\,(\Omega\,cm^2)^{-1}}}\right) + \frac{1000\ \mathrm{K}}{T}\left(-\frac{E_{act,ohm,i}\,\tilde{R}^{-1}}{\mathrm{K}}\right) \quad [13]$$

Consequently, both cell-intrinsic ohmic resistance and contact resistance at the air side can be illustrated in an Arrhenius plot as shown exemplary in Fig. 9 for 0.80 atm H_2O (balanced H_2) and

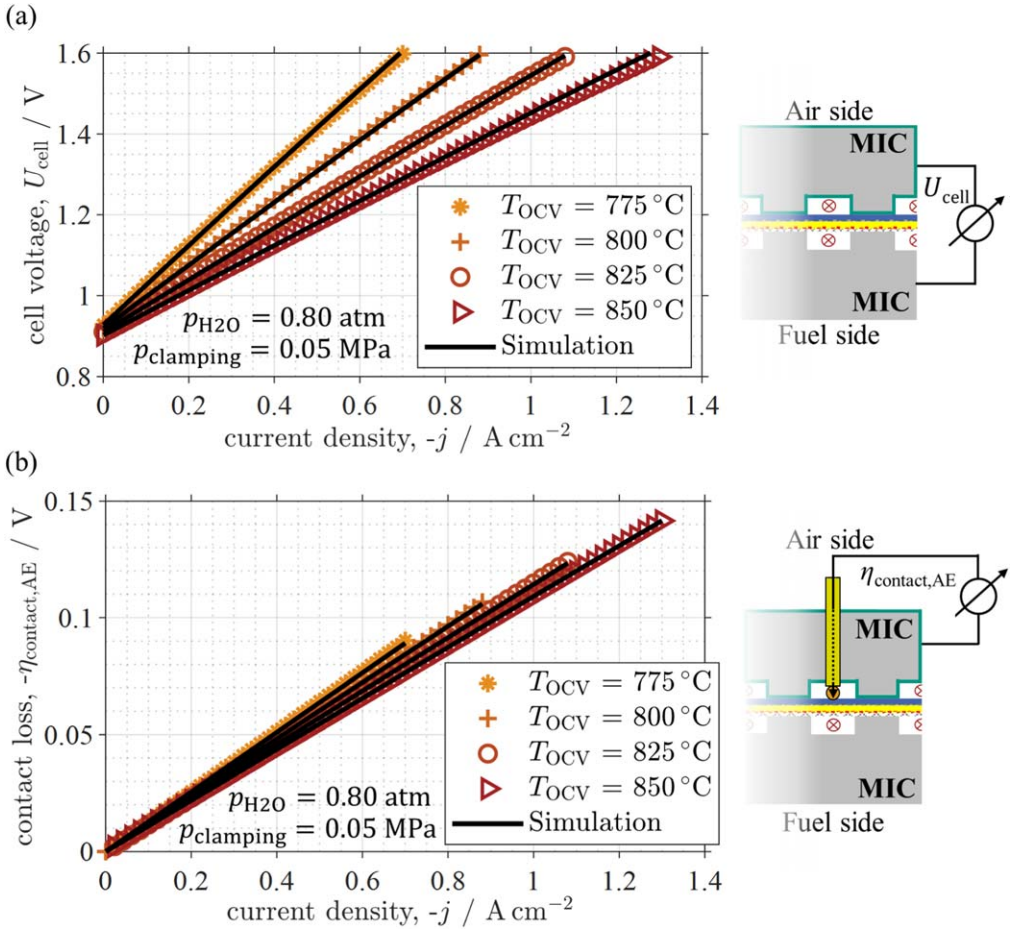

Figure 12. Variation of temperature between 775 and 850 °C with measured as well as simulated (continuous line) (a) current-voltage characteristics and (b) contact losses at the air electrode in SOEC mode with a fuel gas mixture of 0.80 atm H_2O (balanced H_2), oxygen at the air electrode and a clamping pressure of 0.05 MPa.

oxygen at the air electrode with a clamping pressure of 0.05 MPa. By using a linear fit, the parameter $B_{ohm,i}$ can be obtained from the ordinate and $E_{act,ohm,i}$ is ascertainable from the respective slope.

Cell-intrinsic ohmic losses exhibit a dependency on steam partial pressure due to the non-stoichiometry of GDC in the fuel electrode.[48,49] Therefore, the extracted ohmic parameters should include such a dependency for modeling. Consequently, an Arrhenius fit as shown in Fig. 9 is carried out for each measured steam contents, which enables to simulate the cell-intrinsic ohmic parameters over the steam partial pressure at the fuel electrode as illustrated in Fig. 10a for $B_{ohm,cell}$ and 10b for $E_{act,ohm,cell}$. It can be seen that both parameters for both clamping pressures show as a first approximation a linear behavior. Therefore, linear fits are performed in order to obtain functional relationships for modeling, which are shown in Table I.

However, there are differences between 0.05 and 1 MPa regarding the cell-intrinsic ohmic parameter $B_{ohm,cell}$ and activation energy $E_{act,ohm,cell}$. The $p_{H_2O,FE}$-dependency is comparably less pronounced for 1 MPa as for 0.05 MPa. Additionally, $B_{ohm,cell}$ and $E_{act,ohm,cell}$ are comparably lower for 1 MPa, whereby the deviation is decreasing with increasing steam partial pressure.

Since contact losses at the air electrode do not exhibit a dependency towards the steam partial pressure at the fuel electrode, the obtained parameters are averaged here, as shown in Table II. Concerning the ohmic parameter $B_{ohm,contact,AE}$, an increase by a factor of approximately four can be observed from 0.05 to 1 MPa. This is qualitatively in good agreement with Eq. 3, where

Table I. Influence of the clamping pressure towards the cell-intrinsic ohmic parameters with included steam partial pressure dependency for 775 °C $\leqslant T \leqslant$ 850 °C **and** 0.35 atm $\leqslant p_{H_2O,FE} \leqslant$ 0.80 atm**.**

$p_{clamping}$ MPa	$B_{ohm,cell}$ 10^8 K (Ω cm^2)$^{-1}$	$E_{act,ohm,cell}$ kJ mol^{-1}
0.05	$1.3477 - 0.8076 \cdot \frac{p_{H_2O,FE}}{atm}$	$101.12 - 8.42 \cdot \frac{p_{H_2O,FE}}{atm}$
1	$0.4774 - 0.1238 \cdot \frac{p_{H_2O,FE}}{atm}$	$91.64 - 2.55 \cdot \frac{p_{H_2O,FE}}{atm}$

Table II. Influence of the clamping pressure towards the ohmic parameters for the contact losses at the air side for 775 °C $\leqslant T \leqslant$ 850 °C **(error numbers are based on averaging over** 0.35 atm $\leqslant p_{H_2O,FE} \leqslant$ 0.80 atm **with a step width of** 0.15 atm**).**

$p_{clamping}$ MPa	$B_{ohm,contact,AE}$ 10^5 K (Ω cm^2)$^{-1}$	$E_{act,ohm,contact,AE}$ kJ mol^{-1}
0.05	2.462 ± 0.144 (±5.87%)	29.63 ± 0.53 (±1.78%)
1	10.182 ± 0.501 (±4.92%)	29.77 ± 0.48 (±1.45%)

$R_{ohm} \propto B_{ohm}{}^{-1}$, and also to Fig. 6b, where a reduced contact resistance could be evaluated through the increase in clamping pressure. On the contrary, no significant change could be observed for the ohmic activation energy concerning the contact losses at the air electrode $E_{act,ohm,contact,AE}$ in Table II. Therefore, the clamping

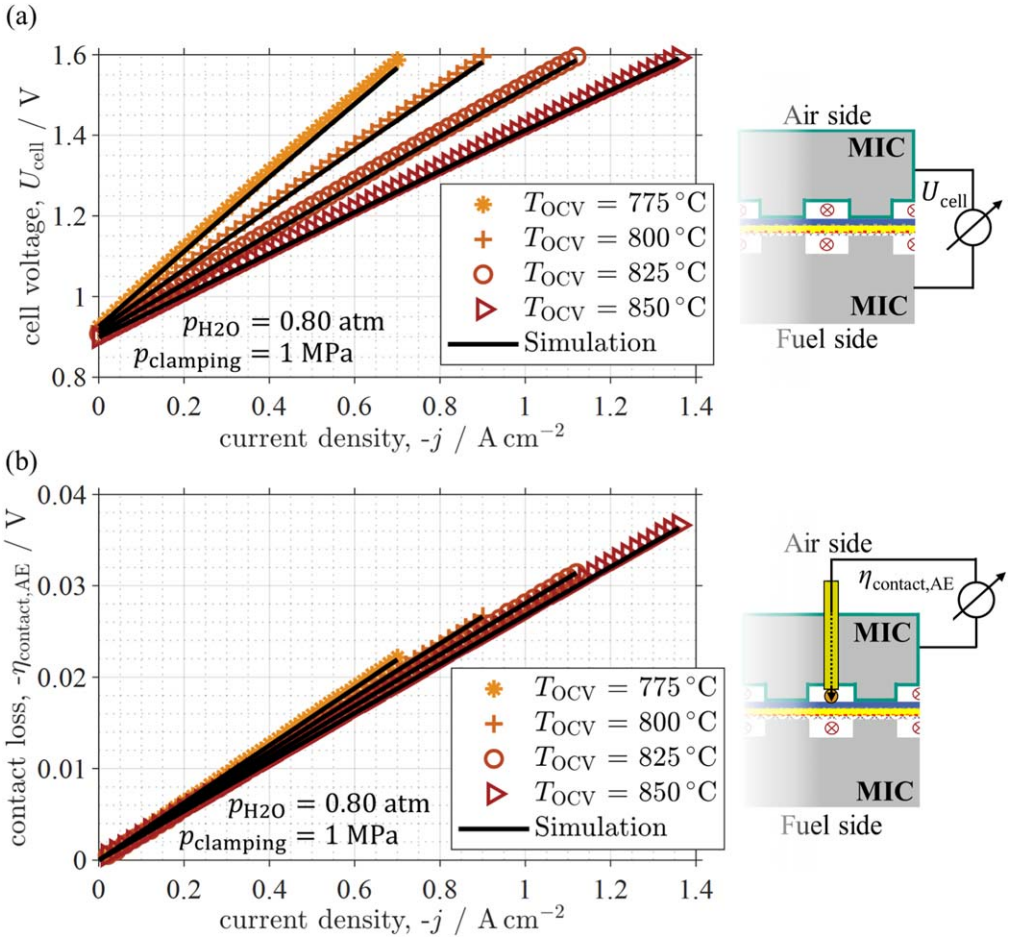

Figure 13. Variation of temperature between 775 and 850 °C with measured as well as simulated (continuous line) (a) current-voltage characteristics and (b) contact losses at the air electrode in SOEC mode with a fuel gas mixture of 0.80 atm H_2O (balanced H_2), oxygen at the air electrode and a clamping pressure of 1 MPa.

pressure seems to have no influence onto $E_{act,ohm,contact,AE}$. Errors resulting from averaging over $p_{H_2O,FE}$ are for both clamping pressures in a similar single-digit percentage range.

With the help of the obtained ohmic parameters from Table II, it is now possible to express the contact resistance at the air electrode in dependence of the temperature. Over $p_{H_2O,FE}$-averaged contact resistances and the corresponding Arrhenius fit with ohmic parameters from Table II are illustrated in Fig. 11 according to Eq. 13. It can be seen for both clamping pressures that the contact resistance at the air electrode $R_{contact,AE}$ is decreasing with increasing temperature. Due to the oxidizing gas atmosphere prevailing at the air side, the surface layer of the MIC consists of metal oxides. The electronic conductivity of such layers is thermally activated,[37] which explains the shown tendency.

After the given zero-dimensional performance model[45] has been extended to stack-like conditions with the previous conducted parameterization, additional adjustments are necessary. Since the flow field geometry differs from the ideal contacting case as shown in Fig. 1, the effective geometry parameter at the fuel side is to be adjusted with the determined values for both clamping pressures from the Appendix. Additionally, pure oxygen was used at the air electrode. Therefore, gas diffusion and activation losses are zero and consequently not considered here. Since the Ni/GDC fuel electrode is the same as in the given model, parameters for the Butler-Volmer equation and exchange current density concerning the fuel electrode are used from Ref. 45 and listed in the Appendix, where also an overview of all parameters is given.

Model validation.—After the zero-dimensional performance model from Ref. 45 has been extended and adjusted to stack-like conditions, the cell voltage can now be modeled according to Eq. 1. In addition, due to the separate parameterization of ohmic losses before, it is now possible to further simulate contact losses at the air electrode.

The model covers operating temperatures from 775 to 850 °C with steam contents between 35 and 80 % at the fuel electrode (balanced with H_2) in a cell voltage range from open circuit voltage to 1.6 V, as only electrolysis mode is considered in this contribution. In order to gain an excellent agreement with the measured IV-characteristics and contact losses, temperature rise due to self-heating of the cell is considered. This was realized by using the cell temperature measured by a thermocouple approximately 2 mm above the cell surface. In addition, the measured open circuit voltage is used to correct minor leakages less than 2 % in the test bench. Exemplary, a validation for both the cell voltage and contact losses at the air electrode with a fuel gas mixture of 0.80 atm H_2O (balanced with H_2) and oxygen at the air electrode in electrolysis mode for a clamping pressure of 0.05 MPa is shown in Figs. 12a and 12b, respectively. At the same conditions, both

the cell voltage and contact losses at the air electrode are validated as well for 1 MPa in Figs. 13a and 13b, respectively.

Within the validity range, both the cell voltage and contact losses at the air electrode can be reproduced at a clamping pressure of 0.05 MPa as well as 1 MPa by the extended and adjusted performance model with a deviation ⩽3 %. Therefore, the simulation and experimental data are in an excellent agreement.

Conclusions

In this work an electrolyte-supported cell exhibiting a Ni/GDC fuel electrode, 3YSZ electrolyte and LSCF air electrode was investigated in a stack-like contacting concept with Crofer 22 APU® interconnectors and an MCO protective coating at the air side. Further, different clamping pressures of 0.05 and 1 MPa in case of an initially dry LSMC contact layer were analyzed.

The increase of the clamping pressure significantly reduced the contact losses at the air side. Additionally, a new methodology was established in order to characterize and parameterize cell-intrinsic ohmic losses and contact losses at the air electrode separately from each other. It was found that the activation energy from the contact losses at the air electrode showed to be independent towards the clamping pressure. This approach enables the extension of an existing zero-dimensional dc performance towards stack-like conditions. Here, the dependency of the cell-intrinsic ohmic losses regarding the oxygen partial pressure dependency of the GDC in the fuel electrode was implemented as well. Modeled cell performance and contact losses at the air electrode are in excellent agreement with experimental data for technically operating conditions.

Acknowledgments

The authors gratefully acknowledge funding from the Federal Ministry of Education and Research (BMBF 03HY124C) and the European Commission via grant agreement 101138488. Further acknowledgment is extended for the open access funding provided by the KIT Publication Fund of the Karlsruhe Institute of Technology, Germany. Sincere thanks are given to Kerafol GmbH for providing the electrolyte substrates as well as to Sunfire GmbH for producing the test cells. The LSCF contact paste was thankfully provided by Norbert Menzler from Forschungszentrum Juelich GmbH, Institute of Energy and Climate Research (IEK), IEK-1: Materials Synthesis and Processing.

Appendix

Gas diffusion process.—Since gas diffusion at the Ni/GDC fuel electrode strongly overlaps with activation processes,[58–63] an approach from Ref. 45 is used where gas diffusion coefficients of a ternary fuel gas mixture consisting of H_2/H_2O/inert gas are modified with the help of nitrogen and helium as inert components. More information about the method itself can be found in Ref. 45 and shall be concisely summarized in the following. High partial pressures of inert gases (e.g. $p_{inert} = 0.85$ atm) and high temperatures (e.g. $T = 850$ °C) need to be set. The resulting difference in polarization resistance between the gas mixtures with helium and nitrogen can be calculated. With the help of this, an effective geometry parameter at the fuel electrode $G_{eff,FE} = \Psi_{FE}/L_{FE}$ with the microstructure parameter Ψ_{FE} and the thickness L_{FE} of the fuel electrode is obtained, which can be used to calculate the gas diffusion resistance for any gas composition at the fuel electrode.

Figure A·1 shows the DRTs of both ternary gas mixtures at $T = 850$ °C with 0.05 atm H_2O and 0.10 atm H_2 (balanced each N_2 or He) at the fuel electrode and oxygen at the air electrode with a clamping pressure of (a) 0.05 MPa and (b) 1 MPa. It can be seen for both clamping pressures that the low frequency peak is shifted towards lower frequencies with increasing resistance when helium is exchanged with nitrogen. This is in agreement with the fact that the respective gas diffusion coefficients are about two times higher in

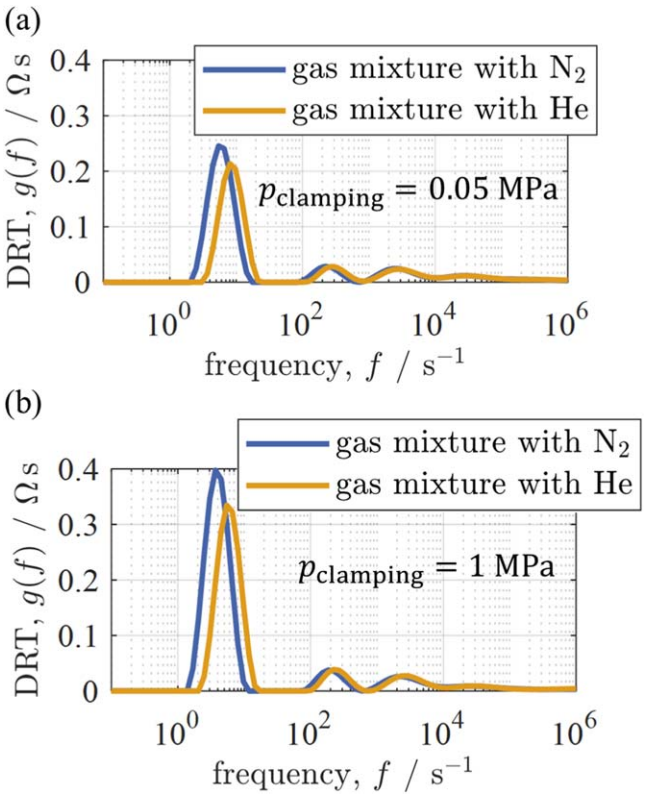

Figure A·1. DRTs of MCO coated MIC and LSMC contact layer with a clamping pressure of (a) 0.05 MPa and (b) 1 MPa at $T = 850$ °C with 0.05 atm H_2O, 0.10 atm H_2 (balanced each N_2 or He) at the fuel electrode and oxygen at the air electrode (MIC = Crofer 22 APU®).

helium than in nitrogen.[45] By comparing both DRTs in Figs. A·1a and A·1b with each other it is becoming clear that the low frequency peaks significantly increase from 0.05 to 1 MPa. This is reflected in the difference in polarization difference and thus in $G_{eff,FE}$. For 0.05 MPa it amounts to 612.78 m^{-1}, while for a clamping pressure of 1 MPa it decreases to 400.56 m^{-1}. Thus, the gas diffusion resistance at the fuel electrode is higher when using a stack-like clamping pressure of 1 MPa compared to 0.05 MPa.

Essentially, gas diffusion at the fuel electrode takes place within the Ni-mesh.[45,59] For this reason, light microscopic images of the used Ni-meshes for both clamping pressures were taken. These are illustrated as color mapped height profiles in Figs. A·2a and A·2b for 0.05 and 1 MPa, respectively. It should be noted that the Ni-mesh within the shown area is in contact with the MIC rib. It can be seen that the height is significantly lower and the wire meshes are thicker for 1 MPa as for 0.05 MPa. Consequently, the Ni-mesh has been compressed by the higher clamping pressure, which results in a smaller volume where in-plane gas diffusion underneath the contact ribs takes place. Therefore, the increased gas diffusion resistance at the fuel electrode might originate from the compressed Ni-mesh.

Additionally, it can be assumed that the increase in clamping pressure would also have an impact on the gas diffusion process at the air side. Consequently, the described inert gas change[45] was also applied there, whereby the decrease in the effective geometry parameter is around 43 % and therefore in a similar scale as at the fuel electrode. One possible cause here might be an enhanced sintering/compression and densification of the porous contact layer through the application of a much higher stack-like clamping pressure of 1 MPa, leading to a reduced porosity and thus increased gas diffusion resistance. However, microstructure analyses are required for a conclusive assessment which is beyond the scope of this work.

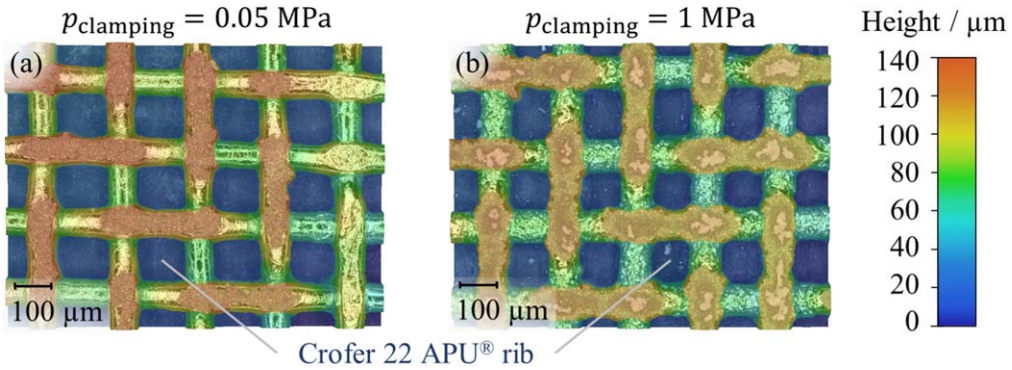

Figure A·2. Post-mortem light microscopic images of the Ni-meshes on the MIC rib illustrated as color mapped height profiles for a clamping pressure of (a) 0.05 MPa and (b) 1 MPa.

Table A·1. Model parameters for the Butler-Volmer equation and exchange current density of the Ni/GDC fuel electrode from Ref. 45.

Parameter	Unit	Value
$a(T = 600 - 750\ °C)$	—	0.035
$a(T = 800 - 900\ °C)$	—	0.161
$b(T)$	—	$0.0012\ K^{-1} \cdot T - 0.9802$
m	—	0.42
$\gamma_{FE}(T)$	$A\ m^{-2}$	$1.46 \cdot 10^5\ (A\ m^{-2}\ K^{-1}) \cdot [(0.8)^{a(T)}(0.2)^{b(T)}]^{-1} \cdot T$
$\alpha_{FE,SOEC}$	—	0.59

Table A·2. Influence of the clamping pressure towards the cell-intrinsic ohmic parameters with included steam partial pressure dependency for 775 °C $\leqslant T \leqslant$ 850 °C **and** 0.35 atm $\leqslant p_{H_2O,FE} \leqslant$ 0.80 atm**.**

$p_{clamping}$ MPa	$B_{ohm,cell}$ $10^8\ K\ (\Omega\ cm^2)^{-1}$	$E_{act,ohm,cell}$ $kJ\ mol^{-1}$
0.05	$1.3477 - 0.8076 \cdot \frac{p_{H_2O,FE}}{atm}$	$101.12 - 8.42 \cdot \frac{p_{H_2O,FE}}{atm}$
1	$0.4774 - 0.1238 \cdot \frac{p_{H_2O,FE}}{atm}$	$91.64 - 2.55 \cdot \frac{p_{H_2O,FE}}{atm}$

Table A·3. Influence of the clamping pressure towards the ohmic parameters for the contact losses at the air side for 775°C $\leqslant T \leqslant$ 850°C**.**

$p_{clamping}$ MPa	$B_{ohm,contact,AE}$ $10^5\ K\ (\Omega\ cm^2)^{-1}$	$E_{act,ohm,contact,AE}$ $kJ\ mol^{-1}$
0.05	2.462 ± 0.144 (±5.87 %)	29.63 ± 0.53 (±1.78 %)
1	10.182 ± 0.501 (±4.92 %)	29.77 ± 0.48 (±1.45 %)

Overview model parameters.—Parameters for the zero-dimensional dc performance model used from Ref. 45 are listed in Table A·1. Further parameters obtained within this work are listed in Tables A·2 and A·3.

Data Availability

The data presented in this manucsript are openly avaiable in the KITopen repository under https://doi.org/10.35097/1972.

ORCID

D. Ewald https://orcid.org/0000-0001-8673-0140
C. Grosselindemann https://orcid.org/0000-0002-9965-843X
D. Esau https://orcid.org/0000-0001-8386-1030
A. Weber https://orcid.org/0000-0003-1744-3732

References

1. J. W. Fergus, *Materials Science and Engineering a-Structural Materials Properties Microstructure and Processing*, **397**, 271 (2005).
2. N. Shaigan, W. Qu, D. G. Ivey, and W. X. Chen, *J. Power Sources*, **195**, 1529 (2010).
3. J. C. W. Mah, A. Muchtar, M. R. Somalu, and M. J. Ghazali, *Int. J. Hydrogen Energy*, **42**, 9219 (2017).
4. D. Udomsilp, C. Lenser, O. Guillon, and N. H. Menzler, *Energy Technology*, **9**, 2001062 (2021).
5. M. E. Ivanova et al., *Angew. Chem. Int. Ed. Engl.*, **62**, e202218850 (2023).
6. A. Hauch, R. Kungas, P. Blennow, A. B. Hansen, J. B. Hansen, B. V. Mathiesen, and M. B. Mogensen, *Science*, **370**, eaba6118 (2020).
7. D. Esau, C. Grosselindemann, S. P. Sckuhr, F. Kullmann, L. Wissmeier, and A. Weber, *ECS Trans.*, **111**, 871 (2023).
8. A. Kromp, A. Leonide, A. Weber, and E. Ivers-Tiffée, *J. Electrochem. Soc.*, **158**, B980 (2011).
9. C. Geipel et al., *ECS Trans.*, **91**, 123 (2019).
10. W. Z. Zhu and S. C. Deevi, *Materials Science and Engineering a-Structural Materials Properties Microstructure and Processing*, **348**, 227 (2003).
11. M. Kornely, A. Neumann, N. H. Menzler, A. Leonide, A. Weber, and E. Ivers-Tiffée, *J. Power Sources*, **196**, 7203 (2011).
12. M. S. Sohal, J. E. O'Brien, C. M. Stoots, V. I. Sharma, B. Yildiz, and A. Virkar, *J. Fuel Cell Sci. Technol.*, **9**, 1 – 10 011017 (2012).
13. M. Stanislowski, E. Wessel, K. Hilpert, T. Markus, and L. Singheiser, *J. Electrochem. Soc.*, **154**, A295 (2007).
14. C. Bernuy-Lopez, U. Bexell, M. Stenstrom, N. Norrby, and J. Westlinder, *ECS Trans.*, **103**, 1803 (2021).
15. N. Gruenwald, D. Sebold, Y. J. Sohn, N. H. Menzler, and R. Vaßen, *J. Power Sources*, **363**, 185 (2017).
16. S. I. Lee, J. Hong, H. Kim, J. W. Son, J. H. Lee, B. K. Kim, H. W. Lee, and K. J. Yoon, *J. Electrochem. Soc.*, **161**, F1389 (2014).
17. A. G. Sabato, E. Zanchi, S. Molin, G. Cempura, H. Javed, K. Herbrig, C. Walter, A. R. Boccaccini, and F. Smeacetto, *J. Eur. Ceram. Soc.*, **41**, 4496 (2021).
18. M. Bianco, S. Poitel, J. E. Hong, S. C. Yang, Z. J. Wang, M. Willinger, R. Steinberger-Wilckens, and J. Van Herle, *Corros. Sci.*, **165**, 108414 (2020).
19. C. Grosselindemann, D. Esau, M. Dorn, F. M. Bauer, L. Wissmeier, and A. Weber, *ECS Trans.*, **111**, 533 (2023).
20. M. Kornely, A. Leonide, A. Weber, and E. Ivers-Tiffée, *J. Power Sources*, **196**, 7209 (2011).
21. X. Montero, F. Tietz, D. Sebold, H. R. Buchkremer, A. Ringuede, M. Cassir, A. Laresgoiti, and I. Villarreal, *J. Power Sources*, **184**, 172 (2008).
22. M. Bianco, J. Tallgren, J. E. Hong, S. C. Yang, O. Himanen, J. Mikkola, J. Van herle, and R. Steinberger-Wilckens, *J. Power Sources*, **437**, 226900 (2019).
23. G. Ghiara, P. Piccardo, V. Bongiorno, C. Geipel, and R. Spotorno, *Energies*, **13**, 6487 (2020).
24. P. Piccardo, R. Spotorno, and C. Geipel, *Energies*, **15**, 3548 (2022).
25. M. C. Tucker, L. Cheng, and L. C. DeJonghe, *J. Power Sources*, **196**, 8435 (2011).

26. M. Kusnezoff, N. Trofimenko, M. Muller, and A. Michaelis, *Materials (Basel)*, **9**, 906 (2016).
27. K. Sick, N. Grigorev, N. H. Menzler, and O. Guillon, *Ceramic Engineering and Science Proceedings*, **39**(2), 99 – 111 (2019).
28. Z. G. Yang, G. G. Xia, P. Singh, and J. W. Stevenson, *J. Power Sources*, **155**, 246 (2006).
29. J. H. Zhu and H. Ghezel-Ayagh, *Int. J. Hydrogen Energy*, **42**, 24278 (2017).
30. X. Montero, F. Tietz, D. Stoever, M. Cassir, and I. Villarreal, *J. Power Sources*, **188**, 148 (2009).
31. M. Kornely, N. H. Menzler, A. Weber, and E. Ivers-Tiffée, *Fuel Cells*, **13**, 506 (2013).
32. J. Froitzheim, S. Canovic, M. Nikumaa, R. Sachitanand, L. G. Johansson, and J. E. Svensson, *J. Power Sources*, **220**, 217 (2012).
33. A. Beez, X. Y. Yin, N. H. Menzler, R. Spatschek, and M. Bram, *J. Electrochem. Soc.*, **164**, F3028 (2017).
34. N. H. Menzler, D. Sebold, and Q. P. Fang, *J. Electrochem. Soc.*, **162**, F1275 (2015).
35. P. Kofstad and R. Bredesen, *Solid State Ionics*, **52**, 69 (1992).
36. M. Palcut, L. Mikkelsen, K. Neufeld, M. Chen, R. Knibbe, and P. V. Hendriksen, *Corros. Sci.*, **52**, 3309 (2010).
37. W. Z. Zhu and S. C. Deevi, *Mater. Res. Bull.*, **38**, 957 (2003).
38. S. Dierickx, T. Mundloch, A. Weber, and E. Ivers-Tiffée, *J. Power Sources*, **415**, 69 (2019).
39. A. Weber, *Tm-Technisches Messen*, **88**, 1 (2021).
40. A. Leonide, V. Sonn, A. Weber, and E. Ivers-Tiffée, *J. Electrochem. Soc.*, **155**, B36 (2007).
41. J. C. Njodzefon, D. Klotz, A. Kromp, A. Weber, and E. Ivers-Tiffée, *J. Electrochem. Soc.*, **160**, F313 (2013).
42. A. Weber, *Tm-Tech. Mess.*, **89**, 97 (2022).
43. A. Leonide, Y. Apel, and E. Ivers-Tiffee, *ECS Trans.*, **19**, 81 (2009).
44. V. Sonn, A. Leonide, and E. Ivers-Tiffée, *J. Electrochem. Soc.*, **155**, B675 (2008).
45. C. Grosselindemann, N. Russner, S. Dierickx, F. Wankmueller, and A. Weber, *J. Electrochem. Soc.*, **168**, 124506 (2021).
46. F. Kullmann, M. Mueller, A. Lindner, S. Dierickx, E. Mueller, and A. Weber, *J. Power Sources*, **587**, 233706 (2023).
47. F. Kullmann, C. Grosselindemann, L. Salamon, F. M. Fuchs, and A. Weber, *Fuel Cells*, **23**, 420 (2023).
48. S. R. Wang, T. Kobayashi, M. Dokiya, and T. Hashimoto, *J. Electrochem. Soc.*, **147**, 3606 (2000).
49. A. Nenning and A. Opitz, *J. Phys.: Energy*, **2**, 014002 (2019).
50. S. B. Beale, M. Andersson, C. Boigues-Muñoz, H. L. Frandsen, Z. J. Lin, S. J. McPhail, M. Ni, B. Sundén, A. Weber, and A. Z. Weber, *Prog. Energy Combust. Sci.*, **85**, 100902 (2021).
51. J. W. Kim, A. V. Virkar, K. Z. Fung, K. Mehta, and S. C. Singhal, *J. Electrochem. Soc.*, **146**, 69 (1999).
52. S. Primdahl and M. Mogensen, *J. Electrochem. Soc.*, **146**, 2827 (1999).
53. H. Geisler, A. Kromp, S. Hirn, A. Weber, and E. Ivers-Tiffée, *ECS Trans.*, **57**, 2691 (2013).
54. D. Klotz, A. Weber, and E. Ivers-Tiffée, *Electrochim. Acta*, **227**, 110 (2017).
55. A. Weber, *Fuel Cells*, **21**, 440 (2021).
56. M. Schoenleber, D. Klotz, and E. Ivers-Tiffée, *Electrochim. Acta*, **131**, 20 (2014).
57. H. Geisler, A. Kromp, A. Weber, and E. Ivers-Tiffée, *J. Electrochem. Soc.*, **161**, F778 (2014).
58. V. A. Rojek-Woeckner, A. K. Opitz, M. Brandner, J. Mathé, and M. Bram, *J. Power Sources*, **328**, 65 (2016).
59. M. Riegraf, R. Costa, G. Schiller, K. A. Friedrich, S. Dierickx, and A. Weber, *J. Electrochem. Soc.*, **166**, F865 (2019).
60. A. Nenning, C. Bischof, J. Fleig, M. Bram, and A. K. Opitz, *Energies*, **13**, 987 (2020).
61. A. Weber, S. Dierickx, N. Russner, and E. Ivers-Tiffée, *ECS Trans.*, **77**, 141 (2017).
62. M. Riegraf, V. Yurkiv, R. Costa, G. Schiller, and K. A. Friedrich, *ChemSusChem*, **10**, 587 (2017).
63. A. Hagen, A. K. Padinjarethil, and J. Heijne, *Electrochim. Acta*, **461**, 142672 (2023).